Received 2 September 2022; revised 3 February 2023; accepted 10 February 2023. Date of publication 22 February 2023; date of current version 8 March 2023.

Digital Object Identifier 10.1109/OJAP.2023.3247491

Fast, Fully-Automatic Characterization of Metallic and Water-Based Threat Objects for Millimeter-Wave Personnel Screening Systems

MOHAMMAD M. TAJDINI[1], MAHSHID ASRI[2], ELIZABETH WIG[3] (Member, IEEE), ANUTHTHARI GAMAGE[2] (Member, IEEE), AND CAREY M. RAPPAPORT[2] (Fellow, IEEE)

[1]Department of Electrical and Computer Engineering, Tufts University, Medford, MA 02155, USA

[2]Department of Electrical and Computer Engineering, Northeastern University, Boston, MA 02115, USA

[3]Department of Electrical Engineering, Stanford University, Stanford, CA 94305, USA

CORRESPONDING AUTHOR: M. M. TAJDINI (e-mail: mmtajdini@gmail.com)

This work was supported by the U.S. Department of Homeland Security (DHS), Science and Technology Directorate under Award 70RSAT18FR0000115.

ABSTRACT Efficient characterization of concealed person-worn objects enhances the security of air travel and reduces the inspection time. Mm-wave nearfield radar can detect metallic objects such as guns or knives, as well as water-based materials that might be associated with peroxide threats. However, it cannot discriminate these potential threats from benign objects to decrease the nuisance alarm rate. Moreover, distinguishing these potential threats from benign objects in the presence of human skin is even more challenging. The authors have previously developed a method using mm-wave imaging to estimate the nominal body contour (NBC) with attached objects. This paper extends the image-processing-based algorithm to identify concealed metallic and water-based objects, as thin as 1 cm, attached to arms, legs, torso, and the pelvic region. The algorithm determines if the anomaly in the image is due to lossless or conductive material seen respectively as a depression or protrusion relative to the NBC. Next, high-loss water-based objects are distinguished from metallic and benign low-loss objects. The developed method is verified experimentally via actual images of human subjects, with foreign attached objects of various types and sizes. The images were captured by the High Definition-Advanced Imaging Technology (HD-AIT) scanner, a laboratory prototype system developed recently by the U.S. Department of Homeland Security (DHS). The developed codes resulted in zero miss and 7% rate of false alarm, while the rest of objects were either characterized correctly or referred to for a secondary pat down. Our method is performed fully-automatically and within a few seconds.

INDEX TERMS Airport security, automatic screening, computational imaging, counterterrorism, inverse scattering, millimeter-wave radar, remote sensing, signal processing.

I. INTRODUCTION

INCREASES in the use of air transportation demands a higher passenger throughput and a faster personnel screening process while also maintaining travel safety [1], [2], [3], [4]. Fast and accurate characterization of both metallic and non-metallic concealed body-worn objects is essential in lowering the secondary checks [5]. Millimeter-wave (mm-wave) imaging systems are broadly used in airports for personnel screening purposes by the U.S. Transportation Security Administration (TSA) [6], [7], [8]. Mm-waves can penetrate many optically opaque materials like clothing, and yet create a clear reflectivity image of the person's body. Also, due to their small wavelengths, mm-waves can produce very high-resolution images [9], [10], [11], [12], [13], [14]. Discriminating between threats and innocent objects plays a key role in lowering false alarms and decreasing secondary pat downs. Detecting benign objects and excluding them from secondary check procedures will help the passenger lines move faster and result in a more efficient screening process [3], [15]. Since terrorist threats

include not only metallic objects but also plastic and liquid explosives, it is imperative to develop efficient algorithms for personnel screening systems to distinguish metals, weak dielectrics, and peroxide/water-based materials [11].

X-ray imaging systems are very effective in detecting metallic objects [16], [17]. However, due to their ionizing effect, they are no longer used for personnel screening [18]. Near field mm-wave imaging systems are the primary means of detecting concealed metallic weapons such as handguns [19]. Various studies have shown that synthetic aperture radar (SAR) images can be used for accurate identification and characterization of weak dielectric objects on the body surface [20], [21], [22]. Recent studies have discussed the feasibility of weak dielectric characterization using a focused continuous wave radar scanning system by developing a ray-based virtual source model [23], [24], [25], [26]. In [27], a geometrical optics forward model has been used to predict the complex permittivity and thickness of body-worn objects via a single frequency multi-reflect-array system. Weatherall et al. have used a similar method to characterize the object's thickness, dielectric constant, and attenuation in a wideband radar working over 18–40 GHz frequency range by fitting the reflectivity to a geometrical optics model [28].

While conventional metal detectors can detect metallic objects easily, these detectors cannot detect peroxide/water-based materials, which appear in many homemade explosives [11]. Studies have suggested mass spectrometry [29], [30], [31], luminescence and fluorescence methods [32], infrared and Raman spectroscopy [29], [30], [33], [34], [35] for the detection of peroxides. Various sensors have been introduced for chronoamperometric detection of the hydrogen peroxide vapor during the security screening process [36], [37]. All of these methods require installation or usage of an extra device for the detection of peroxides in addition to metal detectors.

This paper introduces a fast, fully-automatic algorithm to distinguish person-worn metallic objects from lossy dielectric objects, and to categorize the latter into high-loss water-based, and low-loss benign objects. The proposed method is experimentally validated by applying it to the reconstructed images of objects – as thin as 1 cm, attached to arms, legs, torso, and the pelvic region – captured by the High Definition-Advanced Imaging Technology (HD-AIT). This is a high-resolution laboratory radar prototype, developed recently by the U.S. Department of Homeland Security (DHS), which works over the frequency range of 10–40 GHz [38], [39]. We assume that an automatic target recognition (ATR) system has preprocessed the reconstructed images to determine the presence, location, and size of the attached foreign object. Our image-processing-based algorithm requires no additional measurement to distinguish potential liquid explosives from both metallic threats and benign materials, a significant step for more efficient personnel screening.

In developing the algorithm, we faced two main challenges. The first is that metallic and water-based objects have large dielectric constants which result in high reflectivity, similar to the skin surface. The second complication is that all three categories of conductive materials – metals, lossy water-based, and low-loss objects – cause a similar deformation to the nominal body contour (NBC), i.e., the imaged body surface contour if there were no foreign object. In other words, the object's back surface often cannot be observed in the radar images. To resolve the challenges, we employ our previously established methods for contour extraction and estimation of the NBCs [40], [41], [42], in addition to two important observations: 1) the deformation of the surface contour in the reconstructed images due to conductive foreign objects with respect to the NBC is always seen as a protrusion rather than a depression; and 2) the average image reflectivity of the extracted contours is higher for the region with the affixed metallic or water-based objects, compared to the NBC without the object.

This paper is organized as follows. Section II summarizes the extraction of contours and estimation of NBCs. In Section III, a signal-processing-based algorithm is presented to distinguish conductive from low-loss objects, and to automatically distinguish lossy water-based objects from metallic and benign low-loss objects. Section IV details our empirical analysis for a training library of HD-AIT images, to optimize our algorithm parameters for distinguishing possible liquid from metallic threats. It also presents further numerical results to test the efficiency of the developed algorithm. The paper concludes with Section V.

II. NOMINAL BODY CONTOUR RECONSTRUCTION IN THE PRESENCE OF AFFIXED OBJECTS

Even with a high-resolution screening radar, the precise distinction of the boundary of the body surface is a challenging task. The authors have already developed an automatic, real-time algorithm for wideband mm-wave estimation of the nominal surface contours for different regions of human body [40], [41], [42]. Given an indication of the presence, centroid, and extent of an anomaly attached to a subject's body as established by an automatic target recognition (ATR) preprocessor, the algorithm employs a small-term Fourier circumferential series to estimate the NBCs even in the presence of affixed foreign objects when a portion of the body cross-section may not be captured by the imaging radar. Our reconstruction method is based on the observation that the variation of axial cross-sections of human body is mostly a smooth function of a circumferential angle φ, while the depression or protrusion of the image anomalies due to the attached objects is expected to rapidly vary with respect to φ.

Our algorithm consists of two steps: contour extraction of the screened object and NBC estimation via Fourier approximation. For the first step, a Canny edge detector filter is applied to the noisy 3D reflectivity images obtained by the screening system. A collection of morphological operations turns the binary edges into a single structural object and subsequently into thin minimally connected-shape contours. For

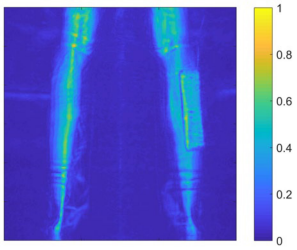

FIGURE 1. The 2D projected image provided by the HD-AIT system of a subject's legs. A rectangular 20×5×2 cm slab of aluminum is affixed to the right calf, and seen best by the ATR processer from the back.

the second step, a seven-term Fourier modal series reconstructs the cross-sectional NBCs, even in the presence of attached objects and when parts of the body are not captured by the imaging system. The deformed contour shows rapid radial variation over angular extent of the object image, which would require more Fourier series terms. The image anomaly due to the object is seen as a distinct depression or protrusion compared to the Fourier series NBC. Even if portions of the body surface are not fully captured by the imaging system, the remaining captured points can be fitted with the seven-term Fourier series to generate a smooth NBC for most parts of the body, even the predominantly triangular cross-section of the knee. The estimation of the NBCs for two body regions which the seven-term Fourier series is unable to fit – the shoulders and the pelvic region – has been discussed in [42]. We have also developed a ranking algorithm to numerically determine the efficiency of the seven-term Fourier decomposition method for the estimation of NBCs [42].

As an example, the developed reconstruction method is applied to estimate the NBC for the right calf of a subject imaged by the HD-AIT system, with an affixed rectangular 20×5×2 cm slab of aluminum viewed best by the ATR processer from the back, as shown in Fig. 1. Fig. 2(a) shows the axial cross-section of the normalized reflectivity at $z = 0.47$ m, with the attached object at the 3 o'clock position, when the subject faces to the left in the direction indicated by the arrow. Fig. 2(b) is the result of applying the Canny edge detector filter, and Fig. 2(c) is the output of the morphological process. Fig. 2(d) illustrates the clean, thin extracted contour. The missing part at 6 o'clock is due to the shadowing by the other leg. The developed Fourier series approximation is applied to find the (black) seven-term Fourier series estimation of the entire NBC, as shown in Fig. 3(a), using the (blue) extracted contour points but excluding both the (red) object region identified previously by the ATR system and the missing data region. The extracted contour and the estimated NBC will be used for characterization of the attached object.

III. CLASSIFICATION OF OBJECTS WITH AN ULTRA-WIDEBAND MM-WAVE SCANNING SYSTEM: A FULLY-AUTOMATIC ALGORITHM

The axial cross-section images acquired via the 3D reconstruction of the HD-AIT screening system output provides quantitative information about the deformation in body surface reconstruction due to the presence of affixed foreign objects. If the deformation of the surface contour appears as a depression in the wideband radar images, the affixed object is automatically classified as lossless [43], [44]. Conductive and lossy affixed materials appear as protrusions, with higher intensity than the NBC of human skin without an affixed object. Benign objects appear as protrusions but tend to have lower loss and lower intensity reflectivity than skin.

Determining whether the object is causing a depression or a protrusion in the image is a necessary step for the identification of metallic and water-based objects. Since the location of the attached object is given by the ATR, one can flag pixels corresponding to the attached object on the extracted contour. The algorithm counts the number of contour pixels that are located inside and outside the NBC, which has been estimated by a seven-term Fourier series. The contour pixels inside the nominal body contour are set to one, and the pixels outside are set to zero. If the number of pixels with the reflectivity level above a certain threshold located inside the nominal body contour is larger than those outside the nominal body contour, the contour will be identified as a depression at the location of the object. If the number of pixels inside and outside the contour are equal, the algorithm fails. Otherwise, the body contour will be identified as a protrusion.

To distinguish metallic and water-based objects from other person-worn objects which also result in protrusion in the images, we propose an algorithm to compare the image reflectivity on the extracted contour for the angular extent of the attached object to the rest of the slice containing the uncovered body part. For each object extent, the reflectivity pixel array is multiplied by a binary array of the corresponding extracted contour. Two metrics are defined to compare the reflectivity level of two extents. The first metric is the maximum reflectivity over the object extent for the 2D image normalized to the maximum reflectivity of the nominal body extent of the considered slice. To develop the second metric, the reflectivity of the object extent is smoothed via a 7-point moving low-pass filter. The average reflectivity of the nominal body extent is computed and called R_{nb}. Subsequently, 90% of R_{nb} is subtracted from the entire image reflectivity. For the object extent, the maximum of the result is calculated and called p_1. For the nominal body extent, the average of the result is computed and called p_2. Finally, the ratio of $\frac{p_1}{p_2}$ is calculated. In this way, we can effectively eliminate the isolated points in the nominal body image with the captured reflectivity levels comparable to the reflectivity level due to the presence of metallic and water-based objects. For both metrics, the same process is performed for all the cross-section slices with the attached object, the average of each metric is computed, and referred to as ratio A and ratio B.

As the object area's extent is given by the ATR system, it may incorrectly include portions of the NBC. Furthermore, for the cylindrical objects, the anomaly feature is seen mostly at its angular mid-point. To have a robust characterization,

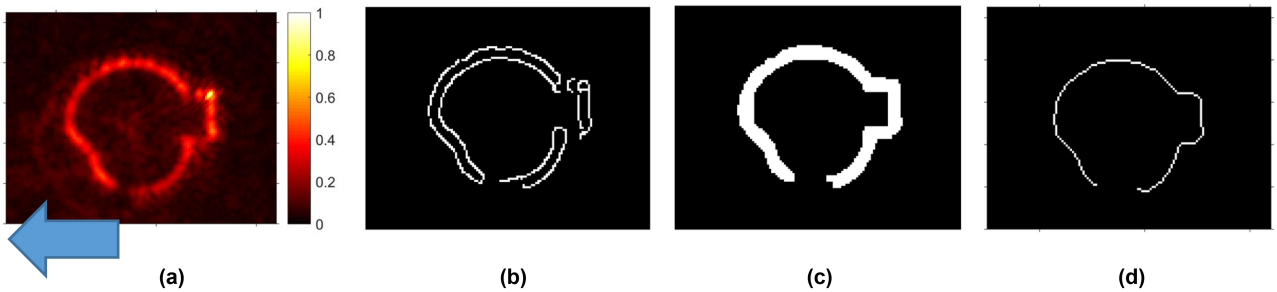

FIGURE 2. The axial cross-sections of the right calf at $z = 0.47$ m with the affixed object of Fig. 1, when the subject viewed from above faces to the left in the direction indicated by the arrow: (a) normalized reflectivity, (b) Canny edge detector filter result, (c) morphological processed result, and (d) the extracted contour. The protrusion is due to the presence of the metallic object. The missing part is due to the shadowing by the other leg.

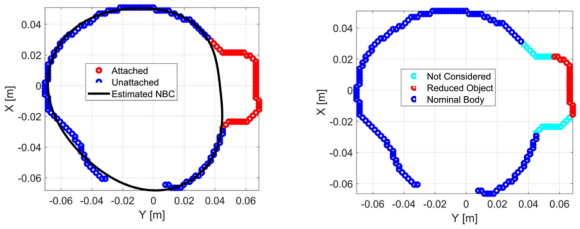

FIGURE 3. Right calf with an affixed slab of aluminum from Fig. 2: (left) the black estimated NBC using a seven-term Fourier series fit to the blue uncovered part of the extracted contour, excluding the red region with the attached slab and also the missing data region, and (right) the red reduced slab region with identical blue nominal body part disregarding the cyan anomaly edges.

the object angular extent is reduced from each side by 25% of the circumferential angle φ, and the ratios A and B are computed only for the middle 50% portion. Fig. 3(b) illustrates the reduced object region contour (red), nominal body part (blue), and neglected pixels at the anomaly edges (cyan). The ratios A and B are calculated only respect to the reduced object region. The entire process is performed fully automatically.

Consistent with electromagnetic theory, our simulation results show that the maximum of the ratios A and B is always lower for lossy water-based objects compared to conductive metals, but higher compared to human skin which in turn is higher compared to benign low-loss objects. A metric M is developed to distinguish metals from water-based materials, and is optimized empirically via a training dataset of the HD-AIT images in the next section.

IV. METALLIC AND WATER-BASED OBJECT DISCRIMINATION WITH AN ULTRA-WIDEBAND MM-WAVE SCANNING SYSTEM: NUMERICAL RESULTS

To differentiate water-based objects from metallic and benign low-loss objects, we analyze a training dataset of reconstructed reflectivity images for various subjects with different heights, weights, and genders wearing different clothing types with a variety of numbers, types, and sizes of concealed attached objects. The optimized parameters of the algorithm are further verified using a second testing dataset. For metallic objects, we investigate the images of aluminum, hex nuts, and irregular objects of interest. We use body lotion and dish soap as simulants of peroxide/water-based threat objects. We also consider honey, 70% isopropyl alcohol, fish oil, and graphite powder as examples of benign low-loss objects.

The 3D reflectivity data is generated by the HD-AIT system via transmitting a wideband signal at each sample point on the 2D aperture, collecting the scattered complex field, and applying a synthetic focusing method [38], [39]. This extremely wide bandwidth will result in five-millimeter depth resolution which enhances the accuracy of object characterization results. The mm-wave readily passes through clothing materials and is reflected by concealed objects as well as the human body, which is highly conductive at mm-wave frequencies [12], [13], [45]. Furthermore, an ATR preprocessor uses one of four 2D projected images with the best view of the attached object, among the front/back/left/right views, to provide the centroid and extent of the body-worn object on a generic human body outline. The preprocess assures a greater privacy by eliminating the need for a TSA officer to analyze the images [46].

A. PARAMETER OPTIMIZATION USING A TRAINING DATASET

The automated codes run on a variety of real-life cases where subjects carried foreign objects attached to different body zones. The training dataset was obtained from measurements with the HD-AIT system. It consists of 41 metallic objects with various shapes, 8 bags of liquid dish soap, 9 bags of graphite powder, and 10 bags of liquid honey. The containers have a variety of shapes of rectangles, circles, squares, and cylinders. The thickness of the attached objects ranges from 1 cm to 6 cm. Both ratios A and B are calculated using the developed automatic characterization algorithm described above. The box plot in Fig. 4 shows clear differences in mean (center line), as well as in overall distribution, between the dish soap and metal. The box plot shows the concentration of calculated ratios for each type of material. Overall, the metallic objects affixed to the body have a higher value using either ratio. The average maximum of ratios A and B for metal and dish soap are 3.7 and 1.7.

Fig. 5(left) shows ratio A for the additional benign object cases of graphite powder and honey. Seven cases were used for graphite powder and eight for honey, in addition to eight dish soap and 42 metal cases. It can be clearly seen that

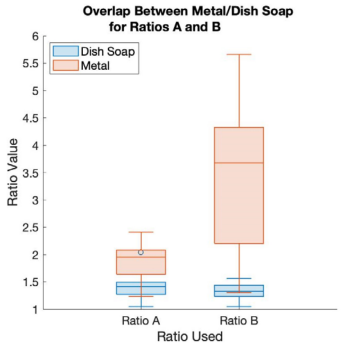

FIGURE 4. Box-plot of ratios *A* and *B* for metal and dish soap cases, showing the mean, 25th and 75th percentiles, and the extension lines showing the maximum and minimum of each value. A single outlier is shown with a dot; the box itself contains the middle 50% of cases.

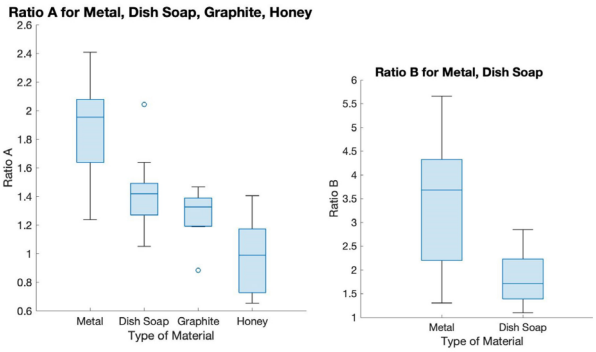

FIGURE 5. (left) Box-plot of ratio *A* for honey, graphite powder, metal, and dish soap, and (right) box-plot of ratio *B* for metal and dish soap. They show clear differences in mean (center line), as well as overall distribution.

while honey and graphite powder have some level of overlap with metal cases at the extrema, their distributions show an overall lower ratio, more similar to dish soap. The salient point from Fig. 5(left) is that graphite and honey have overall lower ratio values than dish soap, meaning that a program that can successfully discriminate between metal and dish soap will also be able to distinguish graphite powder and honey from metal. Ratio B results in a high number of errors for benign objects, but is informative in the case of metals and water-based objects, as is shown in Fig. 5(right). We primarily use ratio A for distinguishing metallic/water-based potential threats from benign objects, and use ratio B to further separate metals from liquid threats. Combining the information from the two ratios A and B was found to offer the best separation between metallic and water-based objects. From these results, and after investigating a variety of threshold parameters, it was determined that using a cutoff of maximum (ratio A, ratio B) $= 1.75$ was the most effective prediction metric for distinguishing between metallic and non-metallic objects. Taking the maximum of the two ratios allowed for more robustness against fluctuations.

To summarize, our numerical investigation shows that for the maximum M of the ratios A and B, if M is higher than 1.75 times the maximum reflectivity intensity of the skin, the target is a metallic object. If M is lower than 1.75 but still higher than 1.2, the target is identified as a water-based object. If M is lower than 1.2 but still results in a protrusion compared to the NBC, the target is a low-loss object. We choose 1.2, not 1.0, to allow for a safety margin of the simulation results.

B. FURTHER NUMERICAL RESULTS FROM A TESTING DATASET

The fully-automatic object characterization algorithm, developed and optimized for a training dataset, is applied in this section to a testing dataset of the actual images of the HD-AIT system. Several numerical examples are presented for different object categories – conductive metals, lossy water-based objects, and low-loss benign objects – attached to different body regions of different subjects, when the HD-AIT measurement data are used for all the tests.

As an example of metallic objects, the developed algorithm is applied to a rectangular 20×5×2 cm slab of aluminum attached to the right calf of a subject, and viewed best by the ATR processer from the back, as shown in Figs. 1 to 3. The contours are extracted from the reflectivity data, the NBCs are estimated via the Fourier circumferential series, and the developed automatic algorithm identifies the anomaly as a protrusion. The ratios A and B are calculated as 1.91 and 2.78. As the maximum of the metrics is above 1.75, the object is characterized correctly as a metallic object.

As another example of characterizing highly conductive metals, a square 13×13×1 cm box of hex nuts (5/16 galvanized) attached to the left ankle of a subject is examined. The 2D projected image of the object viewed best by the ATR processer from the front, the axial cross-section of the normalized reflectivity, and its corresponding NBC is shown in Fig. 6. Applying the developed algorithm, the anomaly is identified as a protrusion. The ratios A and B are calculated as 1.45 and 2.13, which characterize a metallic object. While the ATR processor identifies the front side of the ankle as the attached object region, neglecting the portion of the object on the back, the developed algorithm is sufficiently robust to characterize the object correctly.

As an example of the lossy water-based object characterization, a cylindrical 20×3.5×3.5 cm bag filled with liquid dish soap, attached to the left hip of a subject and viewed best by the ATR from the back, is considered. The 2D projected image of the subject with attached object, the axial cross-sectional image, and the estimated NBC via Fourier series reconstruction are shown in Fig. 7. While the anomaly in the image is identified as a protrusion, the ratios A and B are computed as 1.26 and 1.42, respectively. The maximum of the metrics is above 1.2 but also below 1.75. Consequently, the object is categorized as a water-based object.

As another example of characterizing lossy water-based objects, a circular 14×14×1 cm bag filled with liquid body lotion, attached to the left forearm of a subject and viewed best by the ATR from the front, is examined. The 2D projected image of the subject with attached object, the rotated sagittal cross-section of the normalized reflectivity perpendicular to the axis of the left forearm, and its corresponding

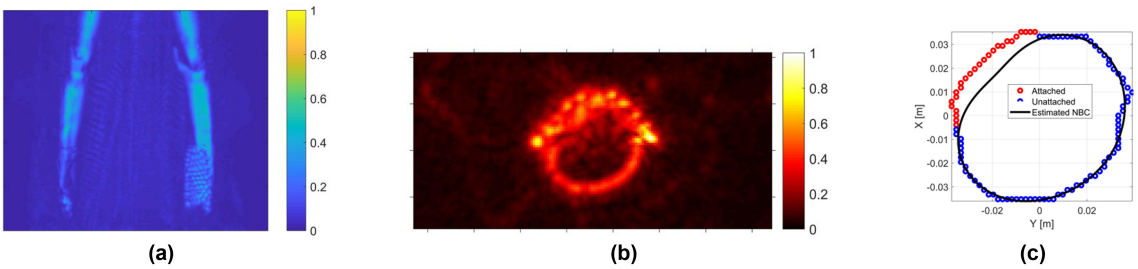

FIGURE 6. A square 13×13×1 cm box of hex nuts (5/16 galvanized) attached at an angle to the left ankle of a subject: (a) the 2D projected image of the subject with the box viewed from the front, (b) the axial cross-section of the normalized reflectivity, and (c) its corresponding contours and NBC. Although the ATR processor identifies the front side of the ankle as the attached object region, neglecting the portion of the object on the back, the developed algorithm is sufficiently robust to characterize the object correctly.

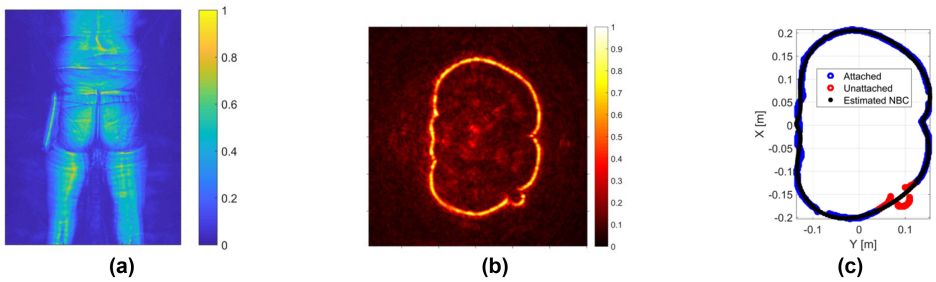

FIGURE 7. A cylindrical 20×3.5×3.5 cm bag filled with liquid dish soap, attached to the left hip of a subject viewed from the back: (a) the 2D projected image of the subject with the attached bag, (b) the axial cross-sectional image, and (c) the contours and estimated NBC via Fourier series.

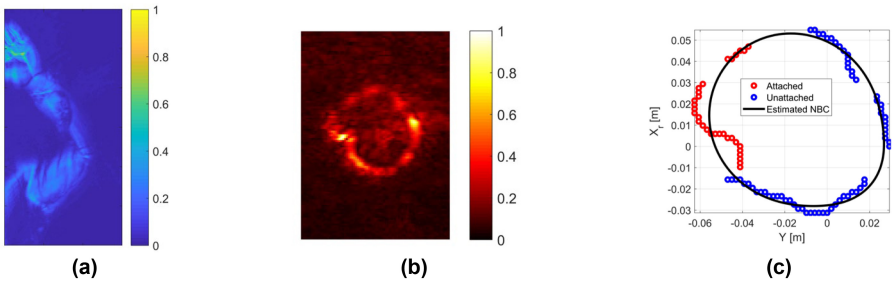

FIGURE 8. A circular 14×14×1 cm bag filled with liquid body lotion, attached to the left forearm of a subject: (a) the 2D projected image of the subject with the attached bag viewed from the front, (b) the rotated sagittal cross-section of the normalized reflectivity perpendicular to the axis of left forearm, and (c) its corresponding contours and NBC. The ATR processor identifies the front side of the left forearm as having an object attached, neglecting the portion of the object on the rear side. Moreover, the extracted contour includes some discontinuities due to the shadowing by the head and left arm and shoulder. Despite the imperfect contours, the developed algorithm is able to provide a continuous NBC, and characterize the material of the body lotion correctly.

NBC is shown in Fig. 8. Applying the developed algorithm, the anomaly is identified as a protrusion. The ratios A and B are calculated as 1.26 and 0.99, respectively, which characterize a water-based object. The ATR processor identifies the front of the left forearm as the attached object region, neglecting the portion of the object on the rear side. Moreover, the extracted contour includes some discontinuities due to the shadowing by the head and left arm and shoulder. Even so, the developed algorithm is able to provide a continuous NBC, and characterize the object correctly. The details of automatically finding the rotated sagittal slices perpendicular to arms/forearms from the set of reconstructed axial slices, in order to compute the corresponding NBCs, have been discussed in [42].

As an example of the benign low-loss object characterization, a square 11×11×1 cm bag filled with graphite powder, attached to the chest of a subject and viewed best by the ATR from the front, is examined. The 2D projected image of the object, the axial cross-sectional image, and the estimated NBC via Fourier series reconstruction are shown in Fig. 9. While the anomaly in the image is identified as a protrusion, the ratios A and B are computed as 1.02 and 0.46, respectively. As the maximum of the metrics is below 1.2, the object is automatically classified as a benign low-loss object obviating a secondary pat down.

As the last example of characterizing innocent low-loss objects, a cylindrical 20×3×3 cm bag filled with liquid honey, attached to the left thigh of a subject and viewed best by the ATR from the left side, is considered. The 2D projected image of the object, the axial cross-sectional image, and the estimated NBC is shown in Fig. 10. While the anomaly in the image is identified as a protrusion, the

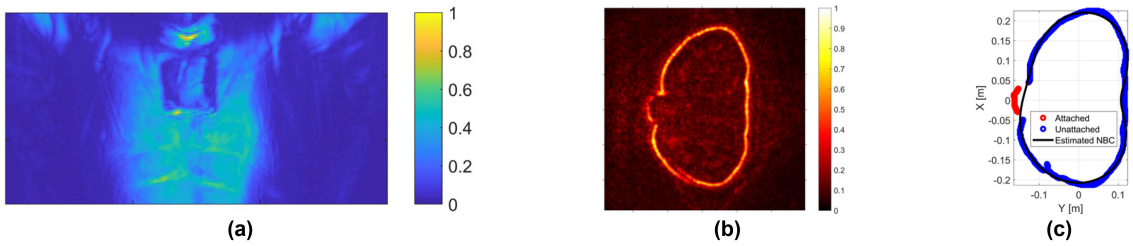

FIGURE 9. A square 11×11×1 cm bag filled with graphite powder, attached to the chest of a subject: (a) the 2D projected image of the subject with the attached bag viewed from the front side, (b) the axial cross-section of the normalized reflectivity, and (c) its corresponding contours and NBC.

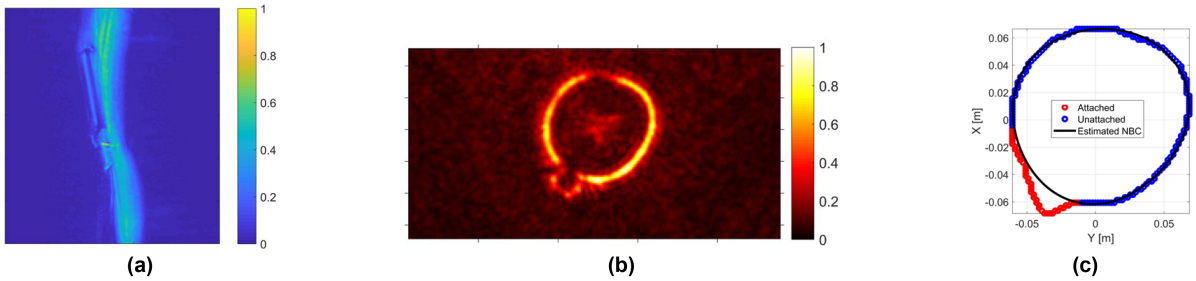

FIGURE 10. A cylindrical 20×3×3 cm bag filled with honey, attached to the left thigh of a subject: (a) the 2D projected image of the subject with the attached bag viewed from the left side, (b) the axial cross-section of the normalized reflectivity, and (c) its corresponding contours and NBC.

ratios A and B are computed as 1.16 and 1.03, respectively. Consequently, the object is flagged as an innocent object, while the entire process is executed fully automatically.

Overall, 30 real-life cases were used as a testing dataset to evaluate the performance of our developed characterization algorithm, consisting of 10 metallic objects (aluminum, hex nuts, and irregular objects of interest), 10 bags of water-based objects (body lotion and dish soap), and 10 bags of benign objects (fish oil, graphite powder, honey, and isopropyl alcohol 70%). Human subjects, with foreign objects wrapped around or otherwise attached to different body zones (arm, torso, pelvic region, knee, calf, and ankle), were screened via the HD-AIT system. The codes ran fully automatically to characterize the body-worn objects. There were 0 miss (labeling a threat object as benign), 2 false alarms (labeling a benign object as a threat), 9 cases when the code could successfully distinguish between metallic, water-based, and benign objects, 2 cases where the water-based object was correctly characterized as a threat but falsely labeled as metallic, and 17 inconclusive classifications (which entail a secondary pat down). Our fully automatic characterization method increases the speed of airport security screening significantly without the need to use different detectors for metallic and water-based objects. No threat object was missed, which indicates the accuracy of the developed algorithm to ensure the safety of airplane passengers.

V. CONCLUSION

We developed an image-processing-based algorithm to characterize concealed metallic and peroxide/water-based threat objects, and distinguish them from benign low-loss objects. The foreign objects used in this research were as thin as 1 cm, and might be attached to or wrapped around arms and forearms, torso and the pelvic region, thighs, calves, and ankles. The entire characterization process is performed fully automatically, and without a need to manual intervention. This results in a lower nuisance alarm rate and better-informed assessments of potential threats. The developed algorithm was validated experimentally by applying it to the actual images of the HD-AIT, a laboratory prototype screening system developed recently by DHS.

The automatic characterization code is executed based on two inputs: 1) the cross-sectional reflectivity images of the mm-wave scanner; 2) the object centroid and extent provided by the ATR preprocessor. For a surrogate water-based object attached to a human knee, the material characterization algorithm takes 3.0 seconds on a personal 4-core laptop with an Intel 1.80 GHz CPU and 16.0 GB RAM.

Our automatic mm-wave characterization method works well for the HD-AIT system, as validated empirically for a testing dataset. A significant risk, however, is that the developed algorithm's optimized parameters (thresholds, contrasts, and limits) are specifically tuned to the utilized training dataset. The algorithm parameters may be recalibrated and further optimized by using updated measured data for a set of different objects or obtained from another set of reference scanner experiments. This task will remain for future work. Our results show a promising solution for enhancing the security of air travel while also speeding up the passenger screening process.

ACKNOWLEDGMENT

The authors would like to thank the reviewers for their constructive comments. The views and conclusions contained

herein are those of the authors and should not be interpreted as necessarily representing the official policies, either expressed or implied, of the DHS.

REFERENCES

[1] J. van Boekhold, A. Faghri, and M. Li, "Evaluating security screening checkpoints for domestic flights using a general microscopic simulation model," *J. Transp. Security*, vol. 7, no. 1, pp. 45–67, Mar. 2014.

[2] A. Knol, A. Sharpanskykh, and S. Janssen, "Analyzing airport security checkpoint performance using cognitive agent models," *J. Air Transp. Manag.*, vol. 75, pp. 39–50, Mar. 2019.

[3] J. Skorupski and P. Uchronski, "Evaluation of the effectiveness of an airport passenger and baggage security screening system," *J. Air Transp. Manag.*, vol. 66, pp. 53–64, Jan. 2018.

[4] A. Pala and J. Zhuang, "Security screening queues with impatient applicants: A new model with a case study," *Eur. J. Oper. Res.*, vol. 265, no. 3, pp. 919–930, Mar. 2018.

[5] P. Corredoura, Z. Baharav, B. Taber, and G. Lee, "Millimeter-wave imaging system for personnel screening: Scanning 10^7 points a second and using no moving parts," in *Proc. Passive Millimeter-Wave Imaging Tech.*, May 2006, Art. no. 62110B.

[6] J. E. Moulder, "Risks of exposure to ionizing and millimeter-wave radiation from airport whole-body scanners," *Radiat. Res.*, vol. 177, no. 6, pp. 723–726, Jun. 2012.

[7] *Passive Millimeter Wave Detectors Market Survey Report*, Dept. Homeland Security's Sci. Technol., SAVER Program, Washington, DC, USA, Jun. 2014.

[8] J. Laviada, M. Lopez-Portugues, A. Arboleya-Arboleya, and F. Las-Heras, "Multiview mm-wave imaging with augmented depth camera information," *IEEE Access*, vol. 6, pp. 16869–16877, 2018.

[9] A. Pedross-Engel, C. M. Watts, and M. S. Reynolds, "A two-sided, reflection-based K-band 3-D millimeter-wave imaging system with image beat pattern mitigation," *IEEE Trans. Microw. Theory Techn.*, vol. 69, no. 11, pp. 5045–5056, Nov. 2021.

[10] D. M. Sheen, D. L. McMakin, H. D. Collins, T. E. Hall, and R. H. Severtsen, "Concealed explosive detection on personnel using a wideband holographic millimeter-wave imaging system," in *Proc. Signal Process., Sens. Fusion Target Recog.*, Jun. 1996, pp. 503–513.

[11] D. M. Sheen, D. L. McMakin, and T. E. Hall, "Three-dimensional millimeter-wave imaging for concealed weapon detection," *IEEE Trans. Microw. Theory Techn.*, vol. 49, no. 9, pp. 1581–1592, Sep. 2001.

[12] S. I. Alekseev and M. C. Ziskin, "Human skin permittivity determined by millimeter wave reflection measurements," *Bioelectromagnetics*, vol. 28, no. 5, pp. 331–339, Jul. 2007.

[13] J. E. Bjarnason, T. L. J. Chan, A. W. M. Lee, M. A. Celis, and E. R. Brown, "Millimeter-wave, terahertz, and mid-infrared transmission through common clothing," *Appl. Phys. Lett.*, vol. 85, no. 4, pp. 519–521, Jul. 2004.

[14] W. Xin, Z. Lu, G. Weihua, and F. Pcng, "Active millimeter-wave near-field cylindrical scanning three-dimensional imaging system," in *Proc. Int. Conf. Micro. MM Wave Techn. (ICMMT)*, May 2018, pp. 1–3.

[15] A. Khazanov and O. Bennis, "Barometric pressure to reduce security false alarms," U.S. Patent 9 940 825, Apr. 2018.

[16] R. F. Eilbert and S. Shi, "Improved imaging for X-ray inspection systems," *IEEE Aerosp. Electron. Syst. Mag.*, vol. 20, no. 3, pp. 23–28, Mar. 2005.

[17] G. Harding, "X-ray scatter tomography for explosives detection," *Radiat. Phys. Chem.*, vol. 71, nos. 3–4, pp. 869–881, Oct. 2004.

[18] *Regulations: Commission Implementing Regulation (EU)*, Official J. Eur. Union, Brussels, Belgium, Aug. 2012.

[19] D. M. Sheen, D. L. McMakin, H. D. Collins, and T. E. Hall, "Near-field millimeter-wave imaging for weapons detection," in *Proc. App. Signal Image Process. Exp. Detect. Syst.*, Apr. 1993, pp. 223–233.

[20] B. Gonzalez-Valdes, Y. Alvarez-Lopez, J. A. Martinez-Lorenzo, F. L. H. Andres, and C. Rappaport, "SAR processing for profile reconstruction and characterization of dielectric objects on the human body surface," *Progr. Electromag. Res.*, vol. 138, pp. 269–282, Jan. 2013.

[21] Y. Alvarez, B. Gonzalez-Valdes, J. A. Martinez-Lorenzo, C. M. Rappaport, and F. Las-Heras, "SAR imaging-based techniques for low permittivity lossless dielectric bodies characterization," *IEEE Antennas Propag. Mag.*, vol. 57, no. 2, pp. 267–276, Apr. 2015.

[22] Y. Alvarez, B. Gonzalez-Valdes, J. A. Martinez, F. Las-Heras, and C. M. Rappaport, "3D whole body imaging for detecting explosive-related threats," *IEEE Trans. Antennas Propag.*, vol. 60, no. 9, pp. 4453–4458, Sep. 2012.

[23] M. Sadeghi, M. M. Tajdini, E. Wig, and C. M. Rappaport, "Single-frequency fast dielectric characterization of concealed body-worn explosive threats," *IEEE Trans. Antennas Propag.*, vol. 68, no. 11, pp. 7541–7548, Nov. 2020.

[24] M. Sadeghi, E. Wig, and C. Rappaport, "Determining the dielectric permittivity and thickness of a penetrable slab affixed to the human body using focused CW mm-wave sensing," in *Proc. IEEE Int. Symp. Antennas Propag. USNC/URSI Nat. Radio Sci. Meeting*, Jul. 2018, pp. 621–622.

[25] M. Sadeghi, E. Wig, A. Morgenthaler, and C. Rappaport, "Modeling the response of dielectric slabs on ground planes using CW focused millimeter waves," in *Proc. 11th Eur. Conf. Antennas Propag. (EUCAP)*, Mar. 2017, pp. 759–763.

[26] M. Sadeghi and C. Rappaport, "Virtual source model for ray-based analysis of focused wave scattering of a penetrable slab on PEC ground plane," in *Proc. IEEE Int. Symp. Antennas Propag. USNC/URSI Nat. Radio Sci. Meeting*, Jul. 2018, pp. 1177–1178.

[27] W. Zhang, H. Gomez-Sousa, J. Heredia-Juesas, and J. A. Martinez-Lorenzo, "Single-frequency imaging and material characterization using reconfigurable reflectarrays," *IEEE Trans. Microw. Theory Techn.*, vol. 69, no. 7, pp. 3360–3371, Jul. 2021.

[28] J. C. Weatherall, J. Barber, and B. T. Smith, "Spectral signatures for identifying explosives with wideband millimeter-wave illumination," *IEEE Trans. Microw. Theory Techn.*, vol. 64, no. 3, pp. 999–1005, Mar. 2016.

[29] H. K. Evans, F. A. J. Tulleners, B. L. Sanchez, and C. A. Rasmussen, "An unusual explosive, triacetonetriperoxide (TATP)," *J. Forensic Sci.*, vol. 31, no. 3, pp. 1119–1125, Jul. 1986.

[30] R. Schulte-Ladbeck, M. Vogel, and U. Karst, "Recent methods for the determination of peroxide-based explosives," *Anal. Bioanal. Chem.*, vol. 386, no. 3, pp. 559–565, Oct. 2006.

[31] J. M. Nilles, T. R. Connell, S. T. Stokes, and H. D. Durst, "Explosives detection using direct analysis in real time (DART) mass spectrometry," *Propellants, Explosives, Pyrotech.*, vol. 35, no. 5, pp. 446–451, Oct. 2010.

[32] M. S. Meaney and V. L. McGuffin, "Luminescence-based methods for sensing and detection of explosives," *Anal. Bioanal. Chem.*, vol. 391, no. 7, pp. 2557–2576, Aug. 2008.

[33] A. J. Bellamy, "Triacetone triperoxide: Its chemical destruction," *J. Forensic Sci.*, vol. 44, no. 3, pp. 603–608, May 1999.

[34] J. Oxley et al., "Raman and infrared fingerprint spectroscopy of peroxide-based explosives," *Appl. Spectrosc.*, vol. 62, no. 8, pp. 906–915, Aug. 2008.

[35] S. P. Stewart, S. E. J. Bell, D. McAuley, I. Baird, S. J. Speers, and G. Kee, "Determination of hydrogen peroxide concentration using a handheld Raman spectrometer: Detection of an explosives precursor," *Forensic Sci. Int.*, vol. 216, nos. 1–3, pp. e5–e8, Mar. 2012.

[36] J. Benedet, D. Lu, K. Cizek, J. La Belle, and J. Wang, "Amperometric sensing of hydrogen peroxide vapor for security screening," *Anal. Bioanal. Chem.*, vol. 395, no. 2, pp. 371–376, Sep. 2009.

[37] J. R. Sempionatto et al., "Wearable ring-based sensing platform for detecting chemical threats," *ACS Sens.*, vol. 2, no. 10, pp. 1531–1538, Oct. 2017.

[38] D. M. Sheen et al., "Wide-bandwidth, wide-beamwidth, high-resolution, millimeter-wave imaging for concealed weapon detection," in *Proc. Passive Active Millimeter-Wave Imag.*, May 2013, Art. no. 871509.

[39] "Passenger screening algorithm challenge." U.S. Department of Homeland Security. [Online]. Available: https://www.kaggle.com/c/passenger-screening-algorithm-challenge

[40] M. M. Tajdini, K. P. Jaisle, and C. M. Rappaport, "Image radar determining the nominal body contour for characterization of concealed person-worn explosives," in *Proc. 14th Eur. Conf. Antennas Propag. (EuCAP)*, Mar. 2020, pp. 1–4.

[41] M. M. Tajdini and C. M. Rappaport, "Determining the nominal body contour image using wideband millimeter-wave radar for characterizing person-worn threats," *Int. J. Microw. Wireless Techn.*, vol. 14, no. 6, pp. 732–738, Jul. 2022.

[42] M. M. Tajdini and C. M. Rappaport, "Nominal body contour reconstruction for millimeter-wave characterization of suicide bomber explosives," *IEEE Trans. Antennas Propag.*, vol. 70, no. 4, pp. 2960–2968, Apr. 2022.
[43] M. Asri and C. Rappaport, "Automatic permittivity characterization of a weak dielectric attached to human body using wideband radar image processing," in *Proc. IEEE Int. Symp. Antennas Propag. USNC-URSI Radio Sci. Meeting*, Jul. 2019, pp. 575–576.
[44] M. Asri, M. Tajdini, E. Wig, and C. Rappaport, "Automatic permittivity and thickness characterization of body-borne weak dielectric threats using wideband radar," in *Proc. 14th Euro. Conf. Antennas Propag. (EuCAP)*, Mar. 2020, pp. 1–4.
[45] D. M. Sheen, "Noise analysis for near field 3-D FM-CW radar imaging systems," in *Proc. SPIE*, May 2015, Art. no. 9462061–7.
[46] J. Accardo and M. A. Chaudhry, "Radiation exposure and privacy concerns surrounding full-body scanners in airports," *J. Radiat. Res. Appl. Sci.*, vol. 7, no. 2, pp. 198–200, Apr. 2014.

MOHAMMAD M. TAJDINI received the B.S. degree in electrical engineering from the University of Tehran, Tehran, Iran, in 2006, the M.S. degree in electrical engineering from Sharif University of Technology, Tehran, in 2008, and the Ph.D. degree in electrical engineering from Northeastern University, Boston, MA, USA, in 2016.

He was a Postdoctoral Researcher with the School of Medicine, University of Maryland, Baltimore, MD, USA, and with the College of Engineering, Northeastern University. He is currently a Research Assistant Professor with the Tufts Institute for Artificial Intelligence (TIAI), Tufts University, Medford, MA, USA. He has also been a Lecturer with Northeastern and Tufts Universities. His research interests include electromagnetic modeling, computational imaging, and machine learning.

MAHSHID ASRI received the B.S. degree in electrical engineering from Iran University of Science and Technology, Tehran, Iran, in 2017, and the M.S. degree in electrical engineering from Northeastern University, Boston, MA, USA, in 2020, where she is currently pursuing the Ph.D. degree. Her work is focused on radar image processing and object characterization. She has completed an internship with Metalenz in 2022.

ELIZABETH WIG (Member, IEEE) received the B.S. and M.S. degrees (*summa cum laude*) in electrical engineering from Northeastern University, Boston, MA, USA, in 2020. She is currently pursuing the Ph.D. degree in electrical engineering at Stanford University, Stanford, CA, USA. She completed internships with Draper in 2017, the NASA Armstrong Flight Research Center, and the NASA Jet Propulsion Laboratory in 2018. She earned the Goldwater Scholarship in 2018, the National Science Foundation Graduate Research Fellowship, the National Defense Science and Engineering Graduate Fellowship, and the Stanford Graduate Fellowship in 2020.

ANUTHTHARI GAMAGE (Member, IEEE) received the B.S. degree in electrical engineering from Tufts University, Medford, MA, USA, in 2018, and the M.S. degree in electrical and computer engineering from the University of Illinois at Urbana-Champaign, Urbana, IL, USA, in 2020. She is currently a Research Associate with the Gordon Center for Subsurface Sensing and Imaging Systems, Northeastern University, Boston, MA, USA.

CAREY M. RAPPAPORT (Fellow, IEEE) received the S.B. degree in mathematics and the S.B., S.M., and E.E. degrees in electrical engineering from Massachusetts Institute of Technology (MIT), Cambridge, MA, USA, in 1982, and the Ph.D. degree in electrical engineering from MIT in 1987.

He has worked as a Teaching and a Research Assistant with MIT from 1981 until 1987, and during the Summers with COMSAT Laboratories, Clarksburg, MD, USA, and the Aerospace Corporation, El Segundo, CA, USA. He joined the Faculty with Northeastern University, Boston, MA, USA, as an Assistant Professor in 1987, where he has been a Professor of Electrical and Computer Engineering since July 2000. In 2011, he was appointed as a College of Engineering Distinguished Professor. In Fall 1995, he was a Visiting Professor of Electrical Engineering with the Electromagnetics Institute, Technical University of Denmark, Lyngby, as part of the W. Fulbright International Scholar Program. In 2005, he was a Visiting Research Scientist with Commonwealth Scientific Industrial and Research Organization (CSIRO), Epping, Australia. He has consulted for CACI, Alion Science and Technology, Inc., Geo-Centers, Inc., PPG, Inc., and several law firms and municipalities on wave propagation and modeling, and microwave heating and safety. He was a Principal Investigator of an ARO-sponsored Multidisciplinary University Research Initiative on Humanitarian Demining, a Co-Principal Investigator of the NSF-sponsored Engineering Research Center for Subsurface Sensing and Imaging Systems (CenSSIS), a Co-Principal Investigator and the Director of the DHS-sponsored Awareness and Localization of Explosives-Related Threats (ALERT), and the Deputy Director of the SENTRY DHS Centers of Excellence. He has authored over 450 technical journal and conference papers in the areas of microwave antenna design, electromagnetic wave propagation and scattering computation, and bioelectromagnetics and has received two reflector antenna patents, two biomedical device patents, and four subsurface sensing device patents.

Prof. Rappaport was awarded the IEEE ANTENNA and Propagation Society's H.A. Wheeler Award for best applications paper, as a student in 1986. He served as an IEEE Distinguished Lecturer from 2016 to 2019. He is a member of Sigma Xi and Eta Kappa Nu professional honorary societies.